



Flexible and superhydrophobic aerogel based on an interpenetrating network of konjac glucomannan and reduced graphene oxide for efficient water–oil separation

Zirong Luo¹, Dandan Li¹, Langhuan Huang^{1,*} , Shaozao Tan¹, and Jiwei Huang¹

¹Guangdong Engineering and Technology Research Centre of Graphene-like Materials and Products, Department of Chemistry, College of Chemistry and Materials Science, Jinan University, Guangzhou 510632, China

Received: 8 March 2020

Accepted: 2 June 2020

Published online:

16 June 2020

© Springer Science+Business Media, LLC, part of Springer Nature 2020

ABSTRACT

Nowadays, the harm caused by the leakage of oil and dangerous organic solvents to the ecological environment and human health cannot be ignored, and effective treatment measures are urgently needed to alleviate the current situation. Therefore, the development of low-cost and efficient adsorbents is the key to solve the problem. In this paper, konjac glucomannan was used as flexible skeleton. Flexible aerogel based on an interpenetrating network of konjac glucomannan and reduced graphene oxide was prepared by two-step hydrothermal method. On this basis, the composite aerogel was superhydrophobically modified to improve its adsorption selectivity. A series of characterization results showed that the adsorbent had flexible three-dimensional porous structure, excellent mechanical properties, adsorption selectivity, recyclability and biodegradability. At the same time, the composite aerogel synthesized by a simple and environmentally friendly method could realize the continuous separation of oil and water by vacuum pump. It showed that its application in the field of high-efficiency oil–water separation had a broad prospect.

Introduction

In recent years, the leakage of oil and dangerous organic solvents has become more and more frequent, which is harmful to the ecological environment and human health [1]. Therefore, the use of

adsorption separation technology to remove organic pollutants in water becomes more and more important [2]. Various materials such as corn stalk [3], cotton [4], activated carbon [5], zeolite [6], nanocellulose [7] and organic polymers [8, 9] have been designed as adsorbents to deal with these pollutions. However, these materials cannot be widely used

Address correspondence to E-mail: thuanglh@jnu.edu.cn

because of their poor adsorption selectivity, high difficulty of recycling and low biocompatibility.

Graphene has been concerned and deeply studied by scientists in various fields because of its outstanding structure and properties. However, it is easy to agglomerate in the process of use due to the strong interaction between two-dimensional graphene sheets [10]. The macroscopic assembly of two-dimensional graphene into three-dimensional graphene aerogel can make full use of the adsorption site. Nevertheless, despite these attractive properties, the practical application of graphene aerogel is limited by its inherent brittleness [11]. The construction of interpenetrating network structure by adding polymer is an vital strategy to improve the brittleness of graphene aerogel [12]. Among the many polymers that act as flexible skeletons, natural polysaccharide biopolymers are especially favored because of their abundant sources, excellent environmental compatibility and biodegradability [13, 14]. Konjac glucomannan is a kind of plant polysaccharides composed of β -1,4 linked D-mannose and D-glucose. It is an excellent skeleton material that has active primary hydroxyl groups in the C-6 position of the skeleton unit and can carry out many interactions such as acylation, carboxymethylation and graft polymerization [15].

In this paper, konjac glucomannan was used as flexible skeleton. Flexible aerogel based on an interpenetrating network of konjac glucomannan (KGM) and reduced graphene oxide (RGO) was prepared by two-step hydrothermal method. On this basis, octadecyl trichlorosilane (OTS) was used as a superhydrophobic modifier to further improve the adsorption selectivity of the composite aerogel. The morphological structure and physicochemical properties of the adsorbent were studied and analyzed by a series of characterization methods. The results showed that the adsorbent had three-dimensional porous structure, excellent mechanical properties, adsorption selectivity, recyclability and biodegradability. In summary, its application in the field of high-efficiency oil–water separation has a broad prospect.

Experimental

Materials

Graphite powder (99.5%) and Sudan red III were purchased from Aladdin Reagent Company. Konjac glucomannan was supplied by Hubei Johnson Konjac Co., Ltd. Sodium nitrate, concentrated sulfuric acid, potassium permanganate, hydrogen peroxide, acetic acid and sodium carbonate were all purchased from Guangzhou Chemical Reagent Factory. The whole process of the experiment was carried out with deionized water. All the common organic solvents used for adsorption test were purchased from Tianjin Damao Chemical Reagent Factory. All the reagents used above were of analytical grade and had no further purification. Vacuum pump oil (density is 0.8795 g/cm³, viscosity is 82.28 mm²/s), engine oil (density is 0.7789 g/cm³, viscosity is 56.31 mm²/s), soybean oil (density is 0.9170 g/cm³, viscosity is 8.36 mm²/s) and diesel (density is 0.8150 g/cm³, viscosity is 6.58 mm²/s) were supplied by Guangzhou Xingsheng Petrochemical Co., Ltd.

Preparation of konjac glucomannan-reduced graphene oxide (KGM-RGO) aerogel by two-step hydrothermal method

Graphene oxide was synthesized by improved Hummer method [16]. KGM powder was dissolved in GO dispersion (5 mg/ml, 20 ml) according to a certain proportion and sonicated for 30 min. Then, the pH of suspension was adjusted to 10 with Na₂CO₃ solution (5 wt%). The fully stirred mixed suspension was loaded into the lining of the polytetrafluoroethylene reactor, and the reactor was placed in a constant temperature reaction chamber at 95 °C for 6 h. After the first step of the hydrothermal reaction, the reactor was reacted at 180 °C for 6 h. After the second step of hydrothermal reaction, the sample was taken out and washed three times with deionized water. Then it was frozen at – 18 °C for 24 h and dried in freeze vacuum at – 55 °C for 24 h to obtain KGM-RGO aerogel. The aerogels prepared with different proportions ($m_{\text{KGM}}: m_{\text{GO}} = 1:2, 1:1, 2:1$) were named KR-1, KR-2, KR-3, respectively. KGM aerogel was prepared by the same method without adding GO.

Preparation of octadecyl trichlorosilane@konjac glucomannan-reduced graphene oxide (OTS@KGM-RGO) aerogel by solution immersion

KGM-RGO aerogel was immersed in 20 ml toluene containing 0.2 g OTS for 30 min and then washed with anhydrous ethanol for three times to remove unreacted precursor molecules. Finally, the sample was dried at 45 °C for 12 h, followed by heating at 120 °C for 1 h to obtain OTS@KGM-rGO aerogel.

Characterizations

In order to explore the chemical structure of the sample, attenuated total reflection Fourier transform infrared spectroscopy (ATR-FTIR) was measured with Bruker Vertex 70 spectrometer, which the scanning range was 550–4000 cm^{-1} . The X-ray diffraction spectrum of the sample was measured by X-ray powder diffractometer (XRD, D/max-12) using Cu K α radiation source ($\lambda = 1.5405 \text{ \AA}$) at the speed of 4°/min. The Raman spectrum of the sample was measured by Raman spectrometer (Renishaw-2000) in the wave number range of 800–3000 cm^{-1} . The wavelength of the exciter was 523 nm. The X-ray photoelectron spectroscopy (XPS) of the sample was determined by ESCALAB-250 photoelectron spectrometer. The microstructure of the sample was observed by field emission scanning electron microscope (FESEM, JEOLJEM-7600F) under 15 kV acceleration voltage, and the sample was sprayed with a thin gold film before the test. The microstructure and element distribution of the samples were characterized by transmission electron microscope (TEM, Philips Tecnai-10) and high-resolution transmission electron microscope (HRTEM, JEOL 2010). The thermal stability of the sample was tested by thermogravimetric analyzer (TG, STA449F3). The sample was heated from room temperature to 600 °C at the rate of 10 °C/min in nitrogen atmosphere. The compression property of the sample was tested by ELF 3220 electronic universal testing machine at the rate of 2 mm/min. In order to test the water–oil wettability of the material, the contact angle of the sample was measured by contact angle tester (CA, SDC-100) at room temperature, and the final result was the average value of the five tests. The weight m and volume V of the sample were measured to calculate the density of the sample.

Performance test methods

The sample was immersed in 200 ml oil or organic solvent for 5 min and then removed until there were no oil droplets behind, which weight was recorded as m_1 (the initial weight of the sample was recorded as m_0). The adsorption capacity of the sample is expressed by the adsorption ratio (AR):

$$\text{AR} = \frac{m_1 - m_0}{m_0} \text{ g/g} \quad (1)$$

The sample immersed in the oil products was taken out at different time intervals (0, 5, 15, 30, 45, 60, 75, 90, 105, 120, 150 and 180 s), and the recorded data were used to make the adsorption kinetic curve. The saturated sample was treated by n-hexane (200 ml) for 4 h and followed by drying in an oven at 40 °C for 6 h before the next cycle adsorption.

In order to test the oil–water selectivity of the sample, diesel oil and carbon tetrachloride were stained with Sudan III and dripped into containers containing deionized water, respectively. The dynamic adsorption of the sample to the oil–water system was observed.

Results and discussion

Preparation of composite aerogel

The schematic diagram of preparation process of composite aerogel is shown in Fig. 1. After two-step hydrothermal method, KGM and GO formed a three-dimensional porous interpenetrating network due to the deacetylation of KGM and the partial reduction of GO. The pure KGM aerogel showed a loose structure compared with the stable KGM-RGO aerogel because there was no interaction between RGO. The superhydrophobic modification of KR-2 aerogel with the most outstanding properties was carried out. The contact angle of the modified OTS@KR-2 reached 150.3°, which density was 0.0114 g/cm^3 .

Chemical composition characterization of composite aerogel

The chemical composition of GO, KGM, KR-1, KR-2, KR-3 and OTS@KR-2 was evaluated by FTIR spectroscopy (Fig. 2a). For GO, the broad band at 3000–3500 cm^{-1} was O–H stretching vibration, and

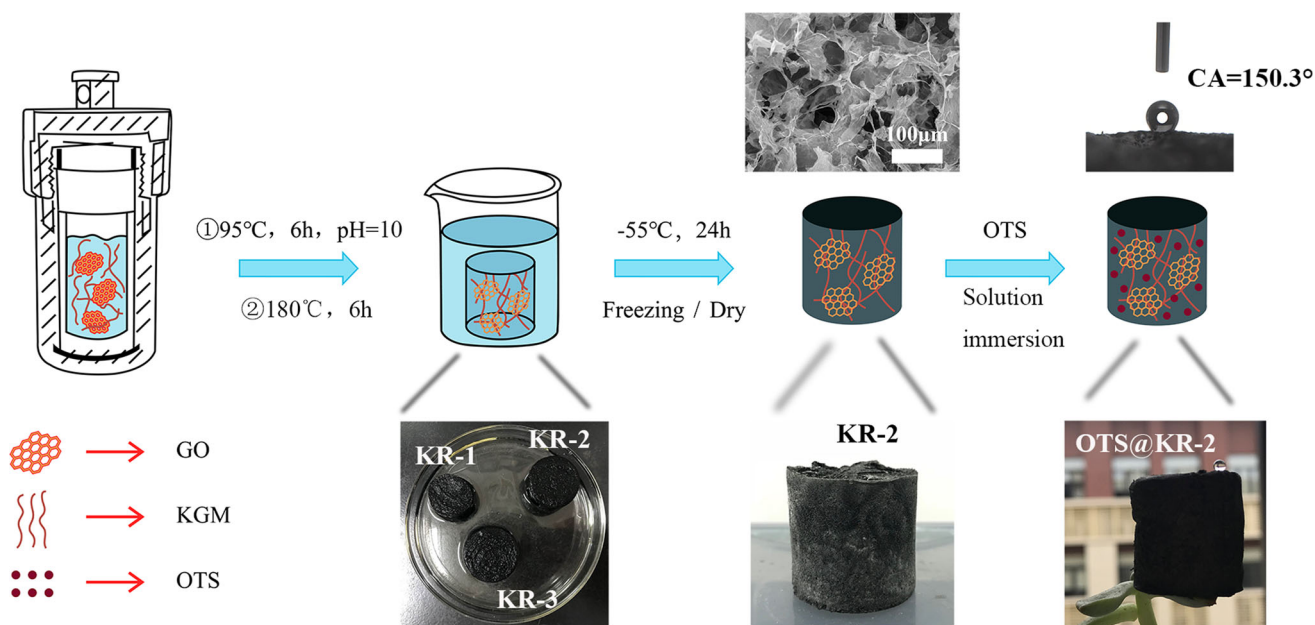


Figure 1 Schematic diagram of preparation process of composite aerogel.

the peaks at 1719 cm^{-1} , 1623 cm^{-1} , 1398 cm^{-1} and 1221 cm^{-1} were corresponded to the C=O vibration peak of carbonyl group and carboxyl group, the C=C stretching vibration peak, the bending vibration peak of O-H group and the respiratory vibration peak of epoxy group, respectively [17, 18]. The peaks of KGM at 3290 cm^{-1} , 2886 cm^{-1} , 1716 cm^{-1} , 1635 cm^{-1} , 1060 cm^{-1} were attributed to -OH, C-H, C=O, C-O, C₆-OH group, respectively. In addition, the absorption band at 807 cm^{-1} was the characteristic vibration of the mannose unit in KGM [19, 20]. Compared with KGM, the intensity of absorption peak of KGM-RGO aerogels at 3290 cm^{-1} and 1635 cm^{-1} decreased obviously, indicating that there was a new hydrogen bond interaction between them after hydrothermal treatment. After OTS treatment, the absorption peaks of the composite aerogel at 2920 cm^{-1} and 2846 cm^{-1} correspond to the asymmetric and symmetrical tensile vibrations of CH₂ and CH₃ from OTS, respectively [21]. The characteristic absorption band of Si-O-Si tensile vibration may overlap with the C-O tensile vibration of polysaccharide unit, resulting in a strong absorption band at about 1026 cm^{-1} .

As shown in Fig. 2b, GO had a narrow and strong diffraction peak at $2\theta = 10.02^\circ$. This peak disappeared in KGM-RGO aerogels, indicating that most of the oxygen-containing functional groups in GO had been removed after hydrothermal reaction,

resulting in a decrease in the distance between nanolayers [22]. The XRD pattern of KGM had a wide characteristic diffraction peak at $2\theta = 14.73^\circ$, which corresponded to its amorphous structure [23]. Compared with KGM, the diffraction peak of KGM-RGO composite aerogel broadened and shifted to the left, which proved that there was an entangled and interpenetrating interaction between RGO and KGM. The XRD pattern of OTS@KR-2 still had a wide peak at $2\theta = 14.73^\circ$. In addition, there was a characteristic peak of NaCl, which might be because the residual Na₂CO₃ in the aerogel reacted with the chloride ion in OTS to form impurities.

The fact that GO was involved in cross-linking and partial reduction could be further proved by Raman spectra. In the Raman spectrum, the D peak is a disordered vibration peak, which represents the disorder between the layers of graphite materials, while the G peak is mainly caused by the in-plane vibration of sp² carbon atoms. The intensity ratio of D peak to G peak (I_D/I_G) usually reflects the structural disorder and defect degree of the material [24, 25]. As shown in Fig. 2c, each material had two characteristic peaks at 1351 cm^{-1} and 1581 cm^{-1} , which corresponded to D peak and G peak, respectively. It can be observed that the I_D/I_G of GO was 0.872, while the I_D/I_G of KR-1 increased to 1.072, which was because part of the oxygen-containing groups of GO fallen off or participated in the cross-linking process. And with

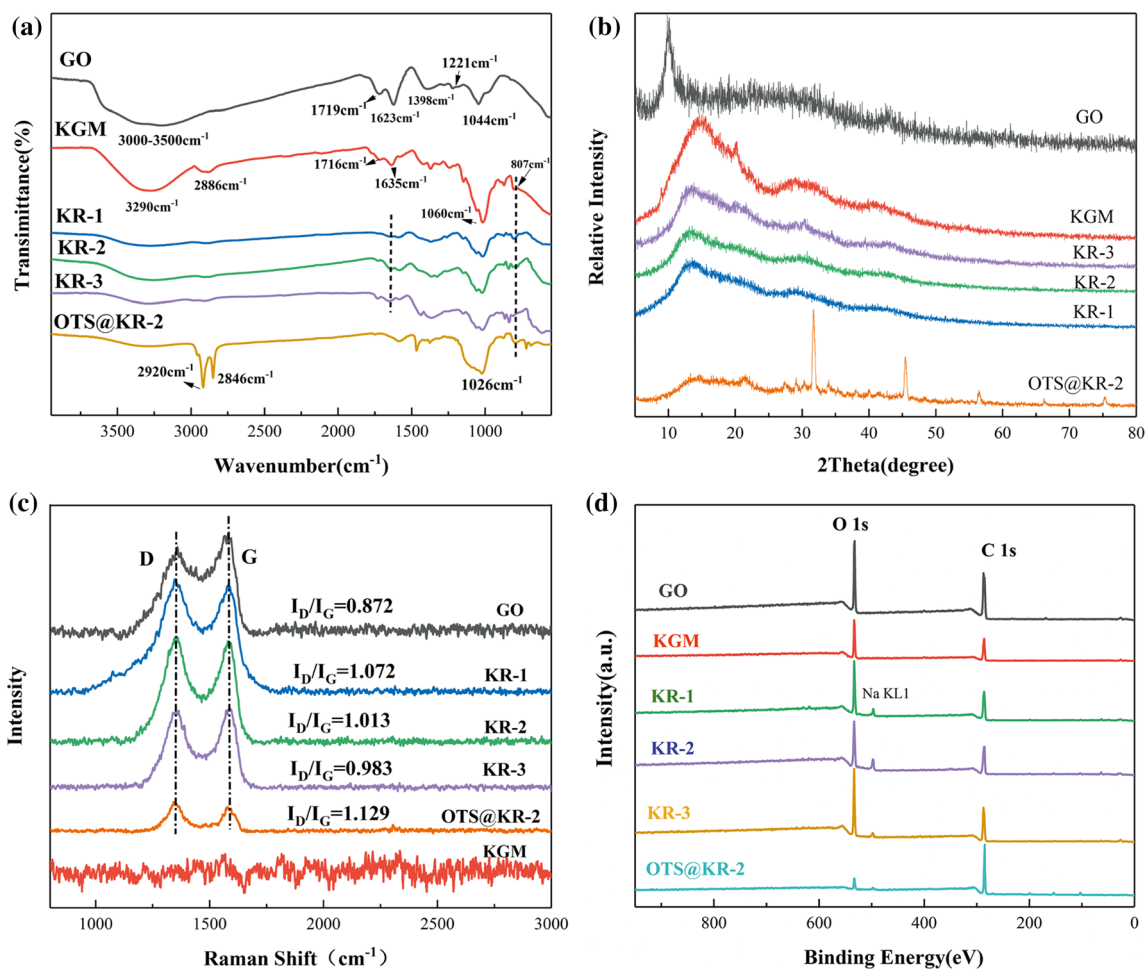


Figure 2 a FTIR spectra, b XRD patterns, c Raman spectra and d XPS spectra of GO, KGM, KR-1, KR-2, KR-3 and OTS@KR-2.

the decrease of the content of GO in KGM-RGO aerogel, the value of I_D/I_G decreased. This showed that the order of the composite aerogel was improved and the defects were reduced due to the interpenetration between KGM and RGO [26]. Due to the existence of OTS, the bimodal intensity of OTS@KR-2 decreased. Its I_D/I_G increased to 1.129, which might be due to the modification of OTS that increased the number of defects in the sample.

The atomic composition and chemical structure of the composite aerogel were further analyzed by XPS. As shown in Fig. 2d, the wide scan XPS spectra of GO, KGM, KR-1, KR-2, KR-3 and OTS@KR-2 showed their C 1s and O 1s peaks at 285.21 and 532.76 eV, respectively. In addition, different proportions of KGM-RGO aerogels had Na KL1 peaks at 497.8 eV. This might be because there was a residue of Na_2CO_3 in the aerogel. After superhydrophobic surface treatment, due to the interaction between OTS and

hydroxyl groups on the surface of KR-2, the O/C atomic ratio decreased from 0.57 to 0.13.

As shown in Fig. 3, the C 1s spectra of GO, KGM, KR-1, KR-2 and KR-3 could be decomposed into three main peaks, which corresponded to the C=O, C–C, C–O bond, respectively. Among them, C=O came from carbonyl group and carboxyl group, and C–O came from epoxy group and hydroxyl group [27, 28]. Under the condition that the contents of C=O and C–O in KR-1 and KR-2 were about the same, the content of C–C in KR-2 was 4.65% higher than that in KR-1. This showed that there were some strong interactions between RGO and KGM after the reaction. With the increase of KGM content, the relative content of C–O in KR-3 increased. As a result, the dense structure formed by KR-3 would collapse to a certain extent due to hydrogen bonding in the presence of water, which was not conducive to the application of oil-water adsorption separation. Because the

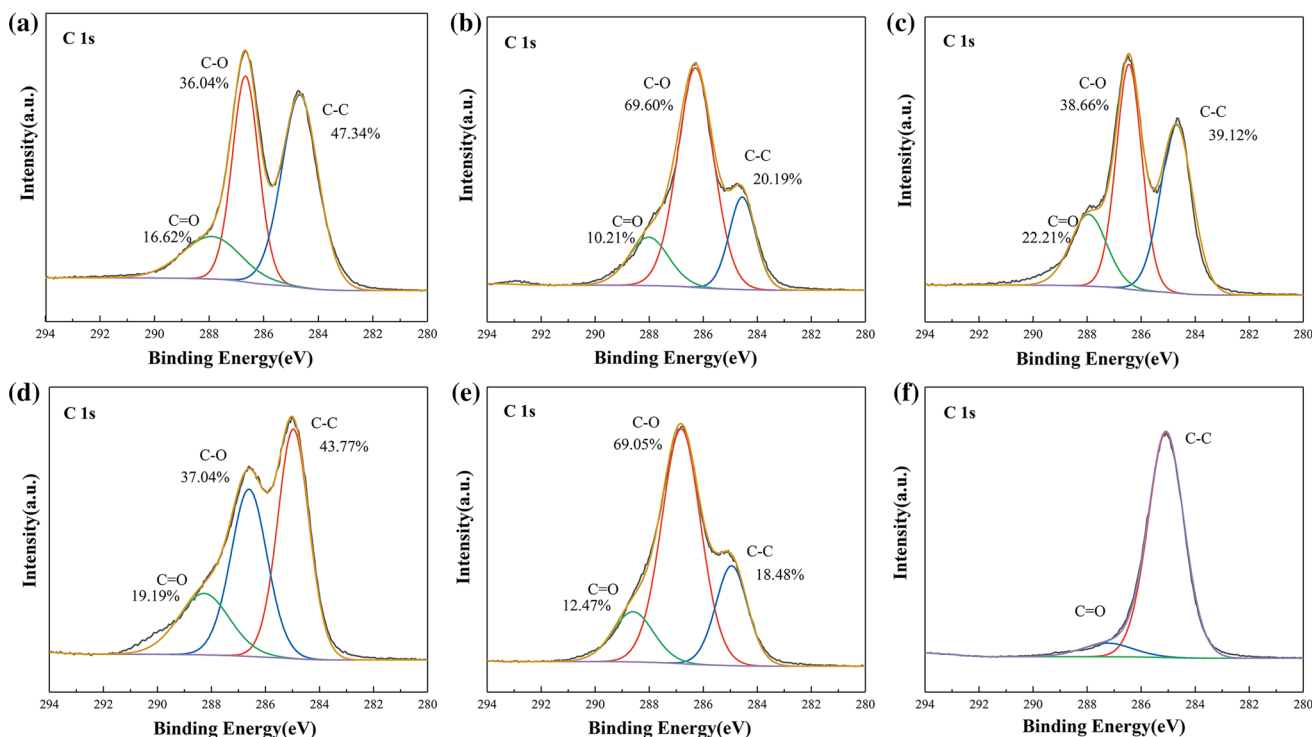


Figure 3 High-resolution C 1s core-level XPS spectra of **a** GO, **b** KGM, **c** KR-1, **d** KR-2, **e** KR-3 and **f** OTS@KR-2.

superhydrophobic treatment consumed a large amount of hydroxyl groups on the surface of KR-2, the relative content of C–C in OTS@KR-2 increased by 49.49% and the relative content of C=O decreased by 12.45%.

Microstructure characterization of composite aerogel

The microstructure of the samples was studied by SEM. Figure 4a shows the internal structure of RGO aerogel, in which could clearly see the formation of layered porous folds. Figure 4b–c shows SEM images of KGM powder and KGM aerogel, respectively. The pure KGM aerogel showed a smooth three-dimensional porous structure with ribbon entanglement. The KR-1 aerogel shown in Fig. 4d formed a denser three-dimensional porous network structure due to the interpenetration of RGO and KGM. More layers and pores appeared on the surface of KR-2 aerogel (Fig. 4e), and the tangled filaments were formed due to the introduction of KGM, yielding a lot of channels. These structures might provide more channels for the transfer of organic matter in the sample during the process of adsorption and separation, thus increasing the adsorption rate. With the increase of

KGM content, the structure of KR-3 was tighter, the surface was rougher, and the pore diameter was smaller (Fig. 4f).

The morphological characteristics of OTS@KR-2 aerogel were evaluated according to SEM, TEM and element distribution map. As shown in Fig. 5a–b that the particle size of OTS particles uniformly distributed on OTS@KR-2 aerogel was 0.5–2 μm after superhydrophobic surface modification. They were attached to the aerogel surface, which could further increase the roughness of the sample. The TEM micrograph of OTS@KR-2 showed that there were black spots on the composite film of RGO and KGM (Fig. 5c). The distribution spectra of carbon (C) atom, oxygen (O) atom, silicon (Si) atom and chlorine (Cl) atom in OTS@KR-2 were confirmed through the energy-dispersive spectrometry (EDS) as shown in Fig. 5d–g. It is known that the main elements on OTS@KGM-RGO were C, O, Si and Cl. The main constituent elements of the black spots were Si and O, which confirmed that OTS had been successfully modified and uniformly distributed on the composite aerogel. This conclusion was consistent with the conclusion obtained by SEM.

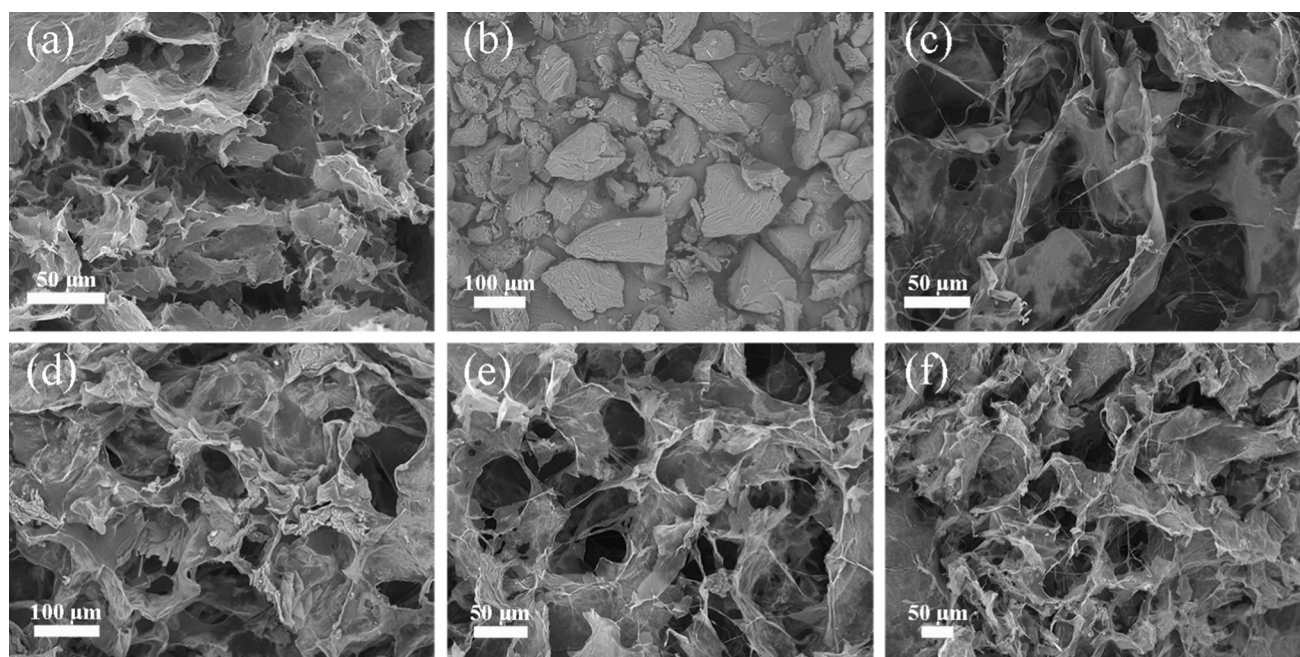


Figure 4 SEM images of **a** RGO aerogel, **b** KGM powder, **c** KGM aerogel, **d** KR-1, **e** KR-2 and **f** KR-3.

Physical and chemical properties of composite aerogel

Compression test was carried out to evaluate the mechanical properties of the samples. Figure 6a shows that when the maximum strain was 40%, the bearable stress of KR-3 was the highest. Meanwhile, with the decrease of KGM content, the bearable stress of KGM-RGO decreased gradually. This indirectly proved that there was a strong force between KGM and RGO, which made them form a close interpenetrating network, and the change of KGM content also affected the strength of this force. In addition, it was found that KR-2 had a certain degree of compressibility. Figure 6b shows the compressive stress–strain curve of KR-2 for multicyclic compression at 40% strain for 10 cycles. After 10 cycles, the stress of the sample decreased, but the structure was not damaged (Fig. 6d). This showed that KR-2 had a good advantage in the recycling of oil–water adsorption separation. In addition, the stress–strain curve of OTS@KR-2 under multicyclic compression at 40% strain was tested (Fig. 6c). It was found that the performance of the sample was not significantly different from that of KR-2 after 10 times of cyclic compression. This showed that the compressibility of the sample was not affected after OTS treatment.

Thermogravimetric analysis of GO, RGO, KGM, KR-1, KR-2, KR-3 and OTS@KR-2 was carried out in

nitrogen atmosphere (Fig. 7). For GO, the loss before 100 °C was mainly due to the evaporation of adsorbed water. The weight loss of 30 wt% occurred at 150–300 °C, which was mainly attributed to the decomposition of oxygen-containing groups [29]. The loss of RGO in the whole heating process (30 wt%) was significantly lower than that of GO, because most of the oxygen-containing groups had been removed in the hydrothermal process. KGM experienced three stages of weight loss. The loss below 100 °C was due to the loss of crystalline water. There was an obvious mass loss (70 wt%) at 150–320 °C, which was caused by the thermal decomposition of oxygen-containing groups in biomass. After 320 °C, the mass loss of the sample was 10 wt% due to the continuous destruction of the structure of KGM molecules [30]. Due to the strong force between KGM and RGO in KR-1 and KR-2, the weight loss in the whole heating process was significantly lower than that of pure KGM, and the thermal stability was significantly improved. With the increase of KGM content, the thermal decomposition curve of KR-3 was similar to that of KGM, but its weight loss was obviously smaller than that of KGM due to the existence of RGO. After superhydrophobic modification, the thermal stability of OTS@KR-2 was obviously higher than that of KR-2 before 400 °C the isolation effect of OTS layer. After 400 °C, the OTS layer was decomposed and

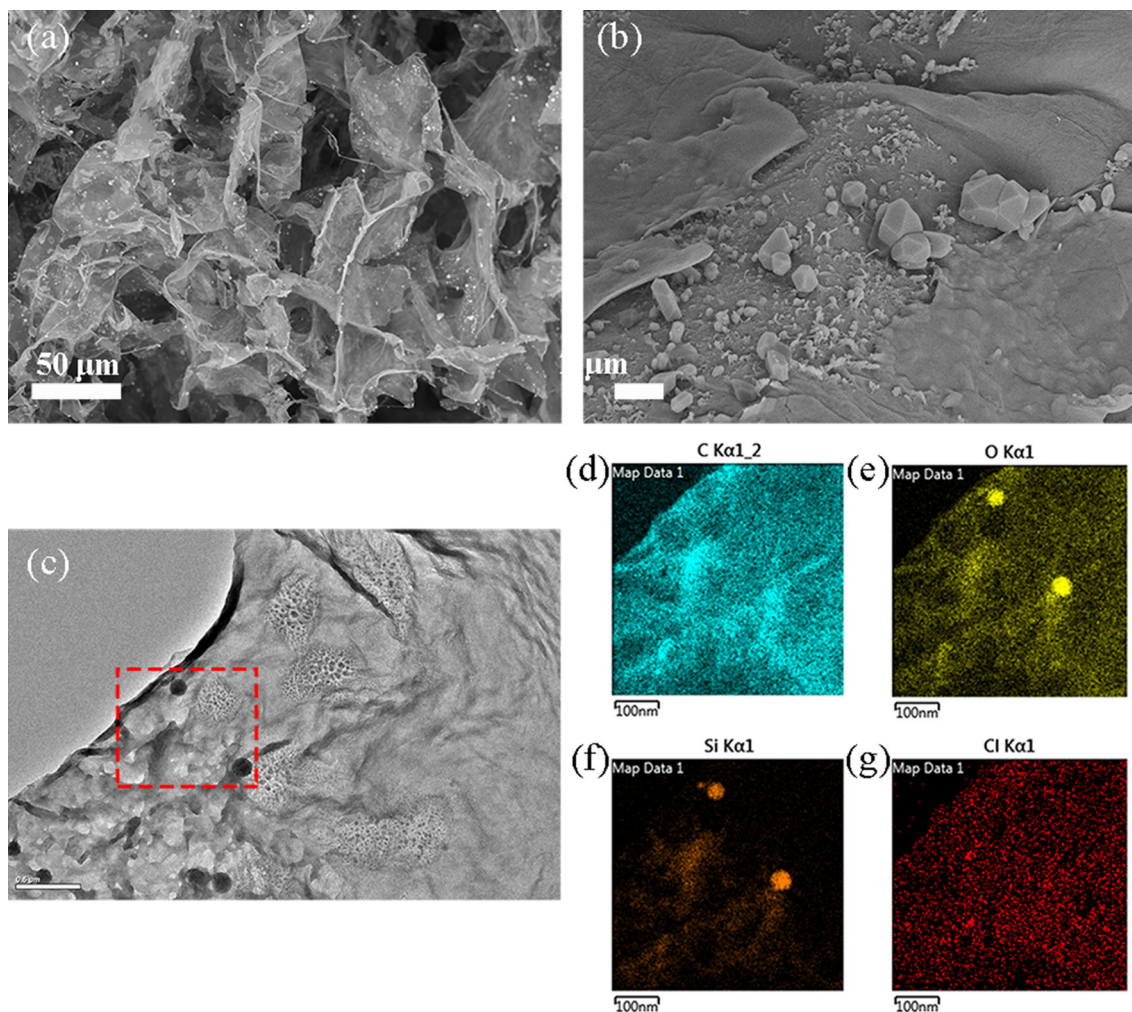


Figure 5 a–b SEM images and c TEM image of OTS@KR-2; d–g elemental distribution mapping of OTS@KR-2, C, O, N and S.

destroyed due to the increase of temperature, and the mass loss was about 25 wt %.

Adsorption properties of composite aerogel

The adsorption capacities of different proportions of KGM-RGO aerogels were studied as shown in Fig. 8a. Obviously, it could be seen from the result that KR-2 had the highest adsorption capacity for four kinds of organic compounds. This might be due to the low content of flexible skeleton in KR-1; the pore structure formed was not mature enough compared with KR-2, which is easy to collapse. With the increase of KGM content, KR-3 had a dense pore structure. However, the adsorption site of the composite aerogel became less and the density increased due to the low content of RGO, which led to the low adsorption capacity. This was consistent with the

conclusion of SEM. In addition, there was no significant difference in the adsorption capacity of the three samples for the pump oil with high viscosity.

The following adsorption properties were tested by KR-2 and OTS@KR-2, because of good mechanical properties and excellent adsorption properties of KR-2. As shown in Fig. 8b, OTS@KR-2 (50.66–90.93 g/g) seemed to perform better than KR-2 (46.42–85.43 g/g) in terms of adsorption capacity for various common oils and organic solvents. This was because after the superhydrophobic surface modification of OTS, the surface of the sample became rougher and the surface energy was lower. This was more beneficial to oil absorption and retention, which led to the increase of adsorption capacity. For some adsorbents (superhydrophobic kapok fiber, CNT/GO sponge, N-doped graphene framework) that did not have compressibility (Table 1), the recovery of oil and the

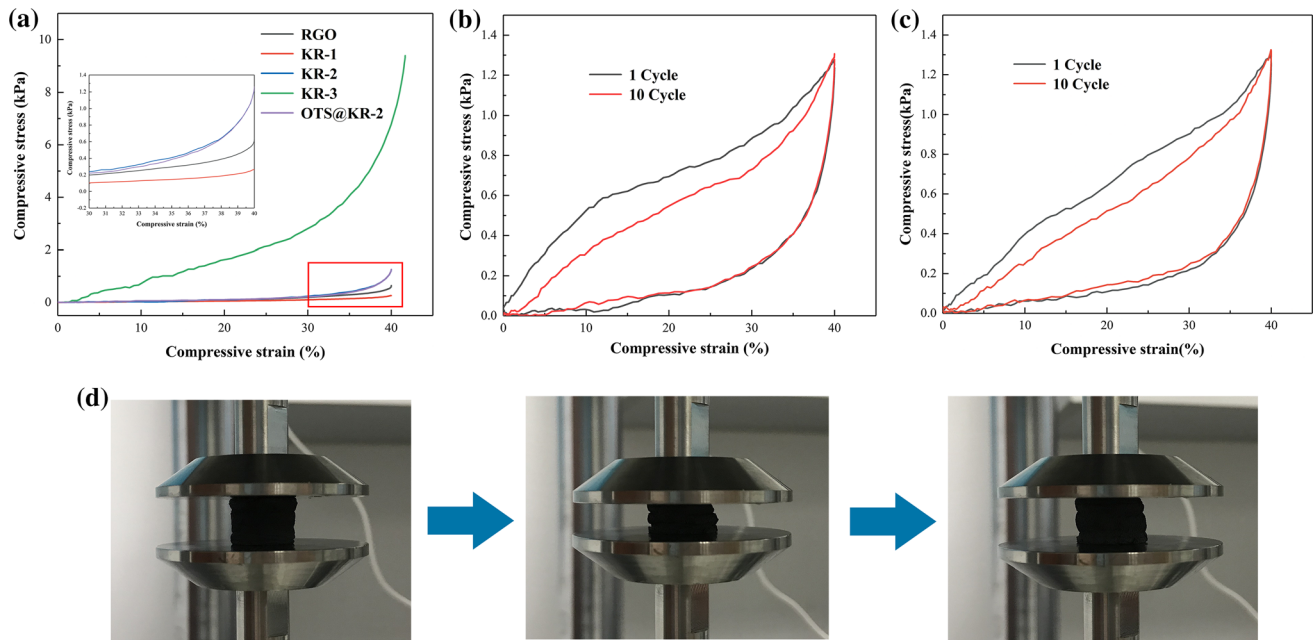


Figure 6 **a** Compressive stress–strain curves of RGO, KR-1, KR-2, KR-3 and OTS@KR-2 at set strain of 40%; compressive stress–strain curve of **b** KR-2; and **c** OTS@KR-2 for multicyclic

compression at 40% strain for 10 cycles, respectively; **d** the digital images of the cyclic compression process of KR-2 using electronic universal testing machine.

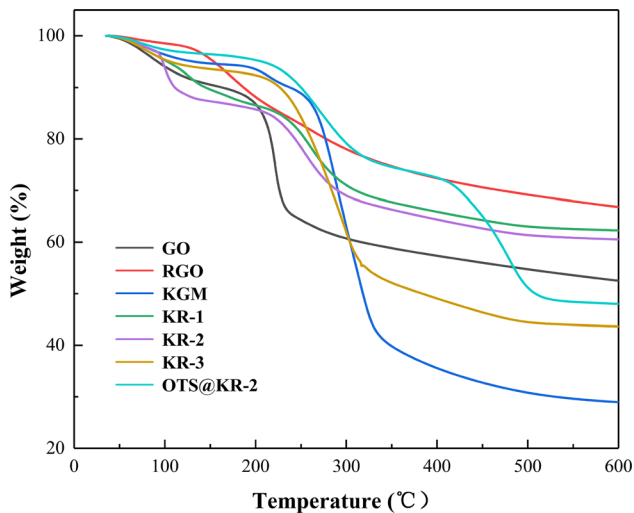


Figure 7 Thermal decomposition curves of GO, RGO, KGM, KR-1, KR-2, KR-3 and OTS@KR-2.

reuse of adsorbents required distillation, combustion, vacuum and other methods. Compared with the simple extrusion method, these methods had high energy output and low efficiency. In addition, some common adsorbents (corn stalk, cotton, reduced graphene oxide foams, PDMS sponge, carbon aerogel) could be recycled by simple methods such as extrusion, but their adsorption capacity was relatively low.

The cycle availability of OTS@KR-2 was tested by 10 cycle adsorption experiments with four model organic compounds. Figure 8c shows that the sample still maintained a high adsorption capacity after 10 adsorption cycles, and the cycle utilization rate reached 99%. Therefore, the OTS@KR-2 in our work was better than some new adsorbents from the comprehensive consideration of adsorption performance and oil recovery and recycling.

In order to further understand the adsorption performance of the sample, the adsorption kinetics curves of OTS@KR-2 for water and several different organic compounds were drawn by intermittent adsorption experiments (Fig. 8d). The adsorption of pump oil, soybean oil, diesel and petroleum ether by OTS@KR-2 reached equilibrium at 90 s, 75 s, 30 s and 15 s, respectively. It could be seen that for the organic compounds with higher viscosity, the adsorption rate of the sample was slower and the adsorption capacity was higher. This might be due to the three-dimensional interpenetrating network structure formed by the composite aerogel, so that the low viscosity model organic matter could be rapidly extended to the whole aerogel along the network structure. At the same time, the sample had high adsorption capacity because the oil with high viscosity could be better attached to the rough surface without reverse

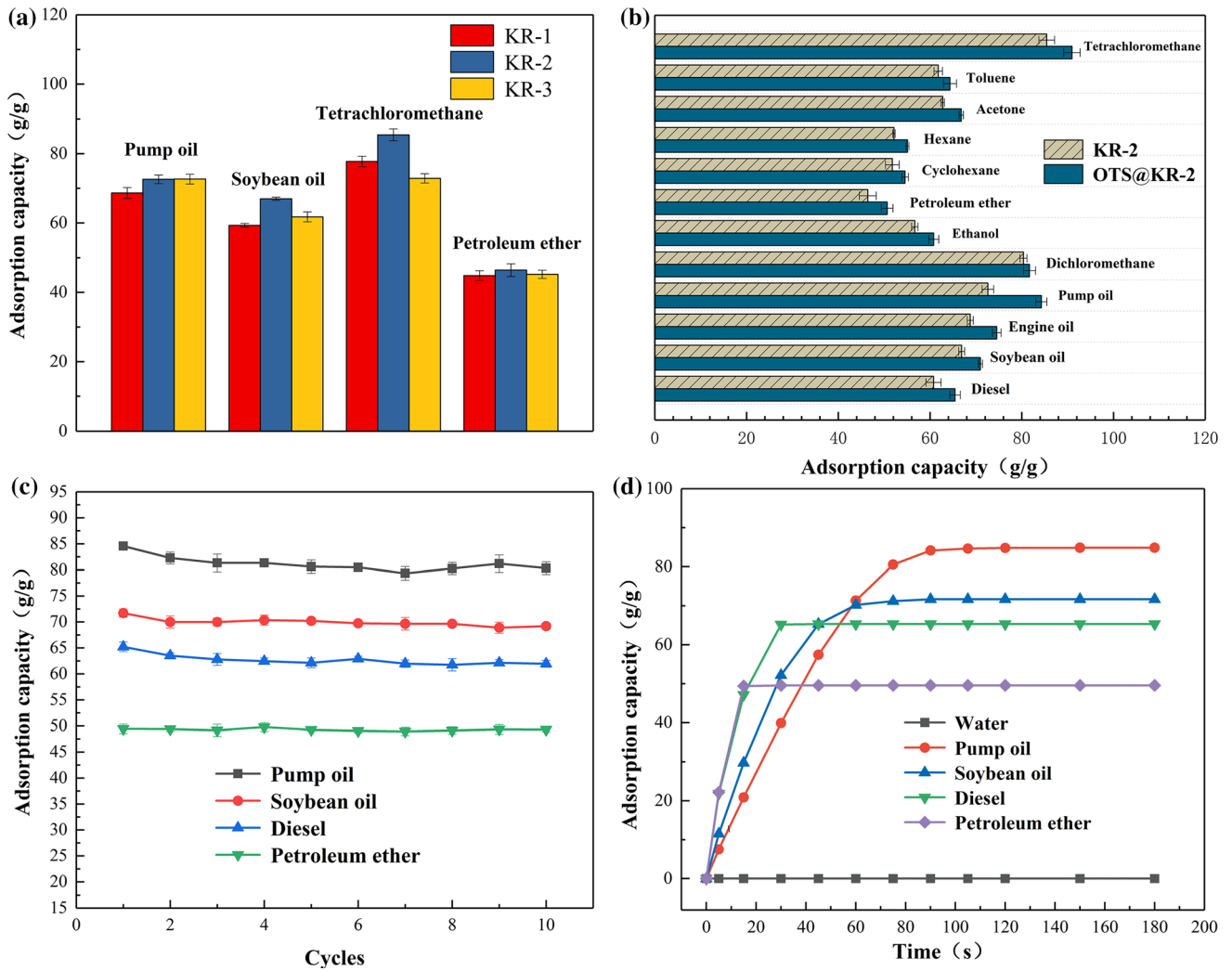


Figure 8 **a** Adsorption capacity of KR-1, KR-2 and KR-3 for pump oil, soybean oil, tetrachloromethane and petroleum ether; **b** adsorption capacity of KR-2 and OTS@KR-2 for various oil products and organic solvents, **c** ten adsorption cycles for pump oil, soybean oil, diesel and petroleum ether by OTS@KR-2; **d** adsorption kinetics curve of four kinds of water and oil products (pump oil, soybean oil, diesel and petroleum ether) by OTS@KR-2.

Table 1 Comparison of adsorption properties of various adsorbents

Adsorbents	Adsorbate	Adsorption capacity (g/g)	Oil recovery and reuse method	References
Corn stalk	Gas oil	8	–	[3]
Cotton	Oils, organic solvents	20–50	Vacuum filtration	[4]
Reduced graphene oxide foams	Oils	5–40	Squeezing	[31]
PDMS sponge	Oils, organic solvents	4–11	Squeezing	[8]
Superhydrophobic Kapok fiber	Oils	48–62	Centrifugal separation	[32]
Cellulose/TiO ₂ aerogel	Paraffin oil	28	Solvent extraction	[33]
Carbon aerogel	Oils, organic solvents	16–50	Distillation	[34]
CNT/GO sponge	Oils, organic solvents	215–743	Heating	[35]
N-doped graphene framework	Organic solvents	200–600	Burning	[36]
OTS@KR-2	Oils, organic solvents	50–90	Squeezing/solvent extraction	This work

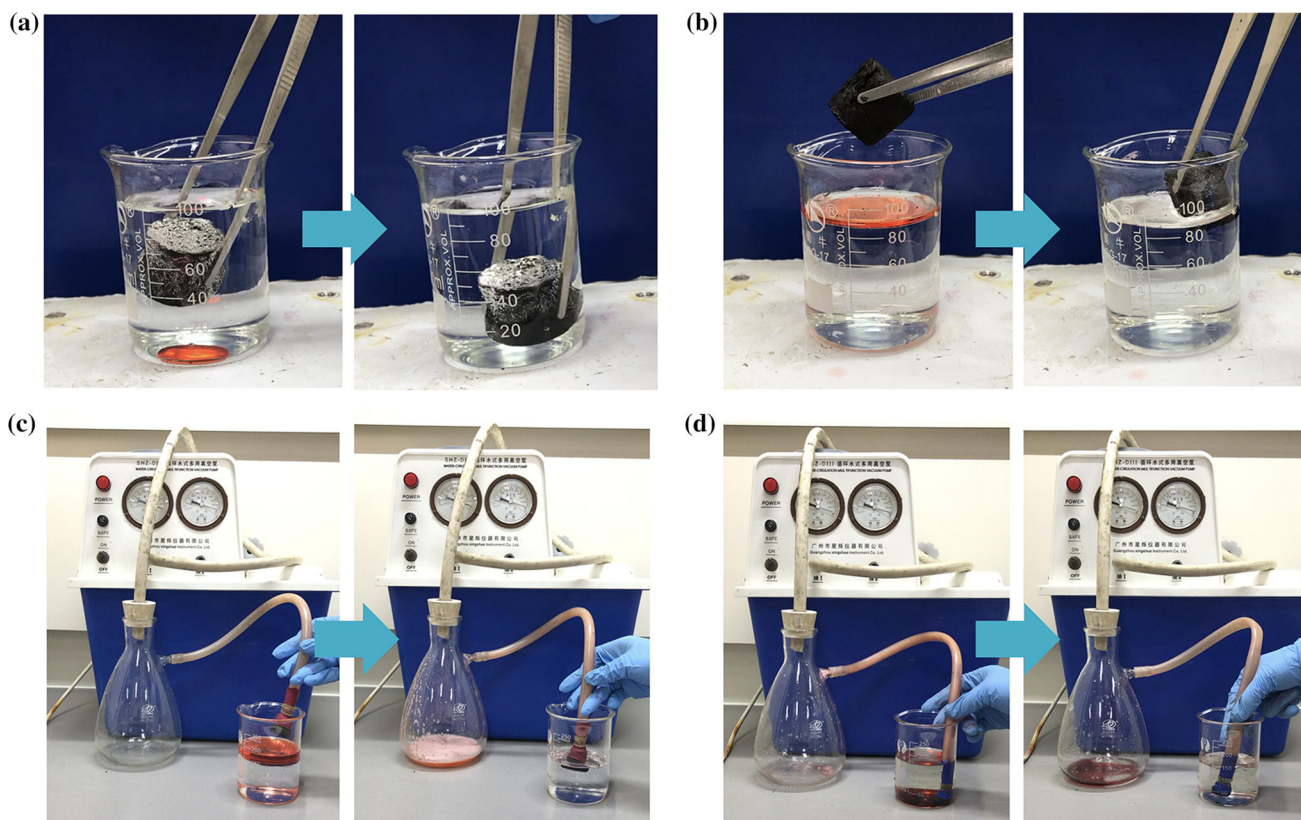


Figure 9 Adsorption and separation process of **a** diesel and **b** tetrachloromethane (both stained with Sudan red III) by OTS@KR-2 in water, respectively; continuous adsorption

separation of **c** diesel and **d** tetrachloromethane (both stained with Sudan red III) by OTS@KR-2 with the aid of pump, respectively.

osmosis. The adsorption capacity of the sample to water had been zero in the corresponding time, which was consistent with the conclusion of superhydrophobicity of the sample.

As shown in Fig. 9a–d, the oil–water separation ability of OTS@KR-2 was tested in a dynamic system by using carbon tetrachloride and diesel (both stained with Sudan red III) as model organic compounds. The phosphorescence on the superhydrophobic surface of the sample was observed in the process of passing through the water layer, and almost all tetrachloromethane at the bottom of the water was adsorbed and removed within 2 s. The diesel floating on the water surface was also absorbed by the sample in a short time, and the water level did not change after the adsorption was completed. The continuous oil–water separation test of the sample was carried out with the help of circulating water vacuum pump. The sample was connected with the vacuum pump tube, which diesel floating on the

water surface and tetrachloromethane sunk at the bottom of the water were collected continuously through the vacuum pump. After the separation process, the water in the beaker had no change, and there was almost no water in the filter bottle except the adsorbed model organic matter, which indicated the excellent oil–water separation ability of the sample. The detailed process can be seen in supplementary video 1, 2.

Conclusions

In this paper, flexible interpenetrating network aerogel based on konjac glucomannan and reduced graphene oxide was prepared by two-step hydrothermal method. The prepared KGM-RGO aerogel had excellent mechanical properties and reusability. The composite aerogels with different proportions showed different toughness, in which

KR-2 showed compressibility due to the appropriate proportion of reticular structure. This was of great significance for the reuse of composite aerogel in adsorption. The superhydrophobically modified composite aerogel (OTS@KR-2) showed better adsorption capacity (50.66–90.93 g/g) and adsorption selectivity ($CA = 145.3^\circ$) while maintaining the original flexible three-dimensional porous structure. In addition, the composite aerogel could realize the continuous separation of oil and water through the vacuum pump. In conclusion, it had a broad prospect in the field of high-efficiency oil–water separation.

Acknowledgements

This work was supported by the National Natural Science Foundation of China (No. 21676116) and the Open Project Supported by Guangdong Engineering & Technology Research Centre of Graphene-Like Materials and Products (GETRCL-201902).

Compliance with ethical standards

Conflict of interest The authors declare that they have no conflict of interest.

Electronic supplementary material: The online version of this article (<https://doi.org/10.1007/s10853-020-04901-2>) contains supplementary material, which is available to authorized users.

References

- [1] Liu H, Geng B, Chen Y, Wang H (2017) Review on the aerogel-type oil sorbents derived from nanocellulose. *ACS Sustain Chem Eng* 5(1):49–66
- [2] Dubansky B, Whitehead A, Miller JT, Rice CD, Galvez F (2013) Multitissue molecular, genomic, and developmental effects of the Deepwater Horizon oil spill on resident Gulf killifish (*Fundulus grandis*). *Environ Sci Technol* 47(10):5074–5082
- [3] Hussein M, Amer A, El-Maghraby A, Hamedallah N (2009) A comprehensive characterization of corn stalk and study of carbonized corn stalk in dye and gas oil sorption. *J Anal Appl Pyrol* 86(2):360–363
- [4] Liu F, Ma M, Zang D, Gao Z, Wang C (2014) Fabrication of superhydrophobic/superoleophilic cotton for application in the field of water/oil separation. *Carbohydr Polym* 103:480–487
- [5] Okiel K, El-Sayed M, El-Kady MY (2011) Treatment of oil–water emulsions by adsorption onto activated carbon, bentonite and deposited carbon. *Egypt J Pet* 20(2):9–15
- [6] Sakthivel T, Reid DL, Goldstein I, Hench L, Seal S (2013) Hydrophobic high surface area zeolites derived from fly ash for oil spill remediation. *Environ Sci Technol* 47(11):5843–5850
- [7] Hamed M, Karabulut E, Marais A, Herland A, Nyström G, Wågberg L (2013) Nanocellulose aerogels functionalized by rapid layer-by-layer assembly for high charge storage and beyond. *Angew Chem Int Ed* 52(46):12038–12042
- [8] Choi S-J, Kwon T-H, Im H, Moon D-I, Baek DJ, Seol M-L, Duarte JP, Choi Y-K (2011) A polydimethylsiloxane (PDMS) sponge for the selective absorption of oil from water. *ACS Appl Mater Interfaces* 3(12):4552–4556
- [9] Oh Y-S, Maeng J, Kim S-J (2000) Use of microorganism-immobilized polyurethane foams to absorb and degrade oil on water surface. *Appl Microbiol Biotechnol* 54(3):418–423
- [10] Wu T, Chen M, Zhang L, Xu X, Liu Y, Yan J, Wang W, Gao J (2013) Three-dimensional graphene-based aerogels prepared by a self-assembly process and its excellent catalytic and absorbing performance. *J Mater Chem A* 1(26):7612–7621
- [11] Wu C, Huang X, Wu X, Qian R, Jiang P (2013) Mechanically flexible and multifunctional polymer-based graphene foams for elastic conductors and oil-water separators. *Adv Mater* 25(39):5658–5662
- [12] Zhu WK, Cong HP, Yao HB, Mao LB, Asiri AM, Alamry KA, Marwani HM, Yu SH (2015) Bioinspired, ultrastrong, highly biocompatible, and bioactive natural polymer/graphene oxide nanocomposite films. *Small* 11(34):4298–4302
- [13] Tan G, Zhou L, Ning C, Tan Y, Ni G, Liao J, Yu P, Chen X (2013) Biomimetically-mineralized composite coatings on titanium functionalized with gelatin methacrylate hydrogels. *Appl Surf Sci* 279:293–299
- [14] Cheng Q, Jiang L, Tang Z (2014) Bioinspired layered materials with superior mechanical performance. *Acc Chem Res* 47(4):1256–1266
- [15] Niu C, Wu W, Wang Z, Li S, Wang J (2007) Adsorption of heavy metal ions from aqueous solution by crosslinked carboxymethyl konjac glucomannan. *J Hazard Mater* 141(1):209–214
- [16] Hummers WS Jr, Offeman RE (1958) Preparation of graphitic oxide. *J Am Chem Soc* 80(6):1339
- [17] Stankovich S, Piner RD, Nguyen ST, Ruoff RS (2006) Synthesis and exfoliation of isocyanate-treated graphene oxide nanoplatelets. *Carbon* 44(15):3342–3347
- [18] Park S, An J, Jung I, Piner RD, An SJ, Li X, Velamakanni A, Ruoff RS (2009) Colloidal suspensions of highly reduced

- graphene oxide in a wide variety of organic solvents. *Nano Lett* 9(4):1593–1597
- [19] Chen J, Liu C, Chen Y, Chen Y, Chang PR (2008) Structural characterization and properties of starch/konjac glucomannan blend films. *Carbohydr Polym* 74(4):946–952
- [20] Nie H, Shen X, Zhou Z, Jiang Q, Chen Y, Xie A, Wang Y, Han CC (2011) Electrospinning and characterization of konjac glucomannan/chitosan nanofibrous scaffolds favoring the growth of bone mesenchymal stem cells. *Carbohydr Polym* 85(3):681–686
- [21] Kumar A, Staněk K, Ryparová P, Hajek P, Tywoniak J (2016) Hydrophobic treatment of wood fibrous thermal insulator by octadecyltrichlorosilane and its influence on hygric properties and resistance against moulds. *Compos B Eng* 106:285–293
- [22] Castarlenas S, Rubio C, Mayoral Á, Téllez C, Coronas J (2014) Few-layer graphene by assisted-exfoliation of graphite with layered silicate. *Carbon* 73:99–105
- [23] Yuan Y, Yang D, Mei G, Hong X, Wu J, Zheng J, Pang J, Yan Z (2018) Preparation of konjac glucomannan-based zeolitic imidazolate framework-8 composite aerogels with high adsorptive capacity of ciprofloxacin from water. *Colloids Surf A* 544:187–195
- [24] Tuinstra F, Koenig JL (1970) Raman spectrum of graphite. *J Chem Phys* 53(3):1126–1130
- [25] Zong Y, Li K, Tian R, Lin Y, Lu C (2018) Highly-dispersed layered double oxide hollow spheres with sufficient active sites for adsorption towards methyl blue. *Nanoscale* 10(48):23191–23197
- [26] Zhu W, Chen T, Li Y, Lei J, Chen X, Yao W, Duan T (2017) High performances of artificial nacre-like graphene oxide-carrageenan bio-nanocomposite films. *Materials* 10(5):536
- [27] Li S, Tao M, Xie Y (2016) Reduced graphene oxide modified luffa sponge as a biocomposite adsorbent for effective removal of cationic dyes from aqueous solution. *Desalin Water Treatment* 57(42):20049–20057
- [28] Chen T, Shi P, Zhang J, Li Y, Duan T, Dai L, Wang L, Yu X, Zhu W (2018) Natural polymer konjac glucomannan mediated assembly of graphene oxide as versatile sponges for water pollution control. *Carbohydr Polym* 202:425–433
- [29] Li N, Yue Q, Gao B, Xu X, Su R (2019) One-step synthesis of peanut hull/graphene aerogel for highly efficient oil-water separation. *J Clean Prod* 207:764–771
- [30] Gan L, Shang S, Hu E, Yuen CWM, Jiang S-x (2015) Konjac glucomannan/graphene oxide hydrogel with enhanced dyes adsorption capability for methyl blue and methyl orange. *Appl Surf Sci* 357:866–872
- [31] Song C, Yin X, Han M, Li X, Hou Z, Zhang L, Cheng L (2017) Three-dimensional reduced graphene oxide foam modified with ZnO nanowires for enhanced microwave absorption properties. *Carbon* 116:50–58
- [32] Wang J, Zheng Y, Wang A (2012) Superhydrophobic kapok fiber oil-absorbent: Preparation and high oil absorbency. *Chem Eng J* 213:1–7
- [33] Chin SF, Romainor ANB, Pang SC (2014) Fabrication of hydrophobic and magnetic cellulose aerogel with high oil absorption capacity. *Mater Lett* 115:241–243
- [34] Li Y-Q, Samad YA, Polychronopoulou K, Alhassan SM, Liao K (2014) Carbon aerogel from winter melon for highly efficient and recyclable oils and organic solvents absorption. *ACS Sustain Chem Eng* 2(6):1492–1497
- [35] Sun H, Xu Z, Gao C (2013) Multifunctional, ultra-flyweight, synergistically assembled carbon aerogels. *Adv Mater* 25(18):2554–2560
- [36] Zhao Y, Hu C, Hu Y, Cheng H, Shi G, Qu L (2012) A versatile, ultralight, nitrogen-doped graphene framework. *Angew Chem Int Ed* 51(45):11371–11375

Publisher's Note Springer Nature remains neutral with regard to jurisdictional claims in published maps and institutional affiliations.